

Exciton–Phonon Coupling of Chiral One-Dimensional Lead-Free Hybrid Metal Halides at Room Temperature

Zhen Li, Yan Yan, Mu-Sen Song, Jia-Yu Xin, Hai-Yu Wang,* Hai Wang,* and Yu Wang*



Cite This: *J. Phys. Chem. Lett.* 2022, 13, 4073–4081



Read Online

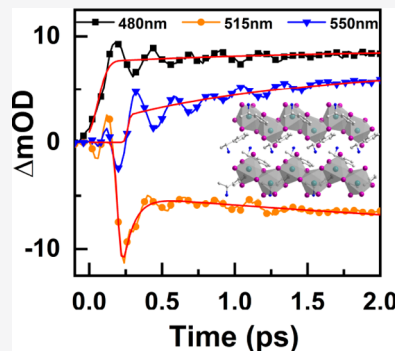
ACCESS |

Metrics & More

Article Recommendations

Supporting Information

ABSTRACT: The interaction between organic cations and inorganic metal halide octahedral units strongly affects the properties of organic–inorganic hybrid metal halides. The “soft” property of the lattice provides the possibility of its strong exciton–phonon interaction. Here we report one-dimensional (1D) lead-free chiral organic–inorganic hybrid metal halide single crystals of (*R/S*)-methylbenzylamine bismuth iodide (*R/S*-MBA)₂Bi₂I₈, which exhibits a high level of octahedral bond distortion. The introduction of chiral amines leads to a strong chiroptical response in the range of 200–600 nm. The strong exciton–phonon coupling can be observed through the coherent oscillation spectrum of transient absorption dynamics at room temperature. The coherent phonon oscillation frequencies are ~97 and ~130 cm^{−1}, corresponding to the symmetrical stretching or bending of the Bi–I octahedron. Our work provides new insights for the study of exciton–phonon coupling in 1D chiral hybrid metal halides.



In recent years, organic–inorganic metal halides have received more and more attention, which as a special category are widely used in photovoltaics,^{1,2} light-emitting diodes (LEDs),^{3,4} lasers,^{5,6} and photodetectors,⁷ due to their superior photoelectric properties, including low trap densities,⁸ long carrier-diffusion lengths,⁹ high photoluminescence quantum yields (PLQYs),¹⁰ tunable absorption and emission wavelengths,¹¹ large Rashba splitting,^{12–14} and long spin lifetimes.^{15,16} Meanwhile, their optical, electronic, and spin properties can also be modulated by the composition of inorganic frameworks and organic molecules and the distortion of bonds and other factors. This flexible crystal structure and ion composition provide the possibility of the introduction of chirality.^{17–20} For example, Billing et al. first reported chiral two-dimensional (2D) perovskite single crystals by incorporating chiral ligands in 2006.²¹ In 2018, Long et al. achieved 3% spin-polarized photoluminescence in reduced-dimensional chiral perovskites without applying an external magnetic field by combining chiral transfer and an energy funneling strategy.²² Tang et al. in 2019 successfully fabricated a direct circularly polarized light (CPL) detector using chiral (*R/S*- α -PEA)PbI₃ (PEA = phenylethylamine) perovskites with an impressive responsivity of 795 mA W^{−1}.²³ Subsequently, Xu et al. fabricated perovskite nanowires of (*R/S*-MPEA)_{1.5}PbBr_{3.5}(DMSO)_{0.5} (MPEA = methylphenethylamine) and demonstrated highly efficient second harmonic generation (SHG) with high polarization ratios and chiroptical nonlinear optical effects.²⁴ Furthermore, the ferroelectric and circularly polarized photoluminescence properties of chiral perovskites have also been reported.^{25–29}

Although chiral metal halides exhibit multiple optoelectronic properties, the chiral luminescence of chiral metal halides is

generally weak. The relative explanation is not clear, which encourages investigation of the mechanism. Recently, a 2D hybrid organic–inorganic perovskite has displayed strong dynamic disorder effects due to the distinct ionic character and the “softness” of the lattice, which influence the optical and electronic properties. However, there have been few studies on the modulation of semiconductor properties by lattice vibration, but understanding the origin and physical processes of phonon modulation is very important for the design and application of materials. For example, Wright et al. investigated the electron–phonon coupling of a three-dimensional (3D) perovskite that is mainly due to the longitudinal optical (LO) phonons scattering via Fröhlich coupling and to the fact that acoustic phonon scattering is negligible near room temperature.³⁰ Debnath et al. found that the formamidinium lead halide (FAPbX₃, where X = Br or I) perovskite nanocrystals (PNCs) generate halide-dependent coherent vibronic wave packets upon above-bandgap nonresonant excitation.³¹ In addition, Sum et al. proved that the exciton fine structure of (PEA)₂PbI₄ 2D perovskite films is modulated by coherent optical phonons dominated by the vibrational motion of the PbI₆ octahedra via deformation potential, which originates from impulsive stimulated Raman scattering.³² The reports mentioned above suggest that exciton–phonon

Received: March 8, 2022

Accepted: April 27, 2022

Published: May 2, 2022

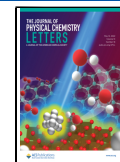


Table 1. Crystal Data and Structural Refinement of $(R\text{-MBA})_2\text{Bi}_2\text{I}_8$, $(S\text{-MBA})_2\text{Bi}_2\text{I}_8$, and $(rac\text{-MBA})_4\text{Bi}_2\text{I}_{10}$

	$(R\text{-MBA})_2\text{Bi}_2\text{I}_8$	$(S\text{-MBA})_2\text{Bi}_2\text{I}_8$	$(rac\text{-MBA})_4\text{Bi}_2\text{I}_{10}$
empirical formula	$\text{C}_{16}\text{H}_{24}\text{Bi}_2\text{I}_8\text{N}_2$	$\text{C}_{16}\text{H}_{24}\text{Bi}_2\text{I}_8\text{N}_2$	$\text{C}_{32}\text{H}_{48}\text{Bi}_2\text{I}_{10}\text{N}_4$
formula weight	1653.34	1653.34	2127.32
temperature (K)		293(2)	
wavelength (Å)		0.71073	
crystal system	orthorhombic	orthorhombic	monoclinic
space group	$P2_12_12_1$	$P2_12_12_1$	$P2_1/c$
unit cell dimensions	$a = 7.6898(6)$ Å $\alpha = 90^\circ$ $b = 13.0048(10)$ Å $\beta = 90^\circ$ $c = 33.332(3)$ Å $\gamma = 90^\circ$	$a = 7.6921(7)$ Å $\alpha = 90^\circ$ $b = 13.0191(11)$ Å $\beta = 90^\circ$ $c = 33.383(3)$ Å $\gamma = 90^\circ$	$a = 14.0624(17)$ Å $\alpha = 90^\circ$ $b = 15.2124(17)$ Å $\beta = 91.861(2)^\circ$ $c = 12.7650(15)$ Å $\gamma = 90^\circ$
volume (Å ³)	3333.3(5)	3343.1(5)	2729.3(6)
Z	4	4	2
density (calculated) (mg/m ³)	3.295	3.285	2.589
absorption coefficient (mm ⁻¹)	17.960	17.907	12.116
F(000)	2800	2800	1832
crystal size	0.18 mm × 0.17 mm × 0.15 mm	0.18 mm × 0.17 mm × 0.15 mm	0.18 mm × 0.16 mm × 0.15 mm
θ range for data collection (deg)	1.68–25.00	2.41–24.99	1.97–25.50
index ranges	$-9 \leq h \leq 9, -15 \leq k \leq 9,$ $-39 \leq l \leq 39$	$-8 \leq h \leq 9, -15 \leq k \leq 15,$ $-39 \leq l \leq 30$	$-17 \leq h \leq 12, -18 \leq k \leq 18,$ $-15 \leq l \leq 15$
no. of reflections collected	19066	19177	16055
no. of independent reflections	5849 [$R_{(\text{int})} = 0.0671$]	5852 [$R_{(\text{int})} = 0.0740$]	5067 [$R_{(\text{int})} = 0.0624$]
completeness to $\theta = 25.00^\circ$ (%)	99.9	99.7	99.7
absorption correction		semiempirical from equivalents	
max and min transmission	0.1737 and 0.1404	0.1742 and 0.1409	0.2637 and 0.2190
refinement method		full-matrix least squares on F^2	
data/restraints/parameters	5849/0/230	5852/0/230	5067/0/193
goodness of fit on F^2	0.905	0.886	1.033
final R indices [$I > 2\sigma(I)$]	$R_1 = 0.0369, wR_2 = 0.0815$	$R_1 = 0.0401, wR_2 = 0.0847$	$R_1 = 0.0442, wR_2 = 0.1009$
R indices (all data)	$R_1 = 0.0451, wR_2 = 0.0856$	$R_1 = 0.0521, wR_2 = 0.0912$	$R_1 = 0.0605, wR_2 = 0.1090$
largest difference peak and hole (e Å ⁻³)	1.442 and -1.299	2.111 and -1.276	1.966 and -1.623

coupling plays an important role in the photoluminescence of chiral metal halides. However, the research on exciton–phonon coupling of metal halides mainly focuses on 2D quantum well-like and 3D bulk materials, and one-dimensional (1D) chain-like inorganic octahedral frames have not been studied.^{33,34} The 1D chiral metal halide samples are obviously different from the relative 2D chiral materials due to the difference in the structure and confined effect, which indicates that there may be different coupling effects in the 1D and 2D chiral materials. Benefiting from the excellent structural stability and a unique 1D enclosed surface, 1D hybrid metal halides have a potential application in optoelectronic devices.³⁵ Moreover, 1D hybrid metal halides with unusual photophysical properties arising from their strong quantum confinement are also expected to be important functional materials for fundamental photophysical research.³⁶ More importantly, the interaction between excitons and phonons is difficult to monitor and usually requires a low-temperature test condition, which makes its research difficult.^{32,37} Therefore, investigating the exciton–phonon coupling of 1D chiral lead-free metal halides is very important, which can provide fresh insights for the development of emerging optoelectronics.

Here we report the synthesis of two 1D lead-free chiral organic–inorganic hybrid metal halide single crystals: (*R/S*)-methylbenzylamine bismuth iodide $(R/S\text{-MBA})_2\text{Bi}_2\text{I}_8$ and racemic $(rac\text{-MBA})_4\text{Bi}_2\text{I}_{10}$. The chiral crystals adopt the edge-sharing $[\text{BiI}_6]^{3-}$ octahedron to form a long 1D chain

structure, and the octahedra have a high level of distortion. A strong circular dichroism (CD) response in the wavelength range of 200–600 nm indicates that the chirality of organic cations can be directly transferred to the inorganic Bi–I sublattice framework. In particular, strong exciton–phonon coupling can be clearly and intuitively reflected from the coherent oscillation in the transient absorption kinetics by circular polarized femtosecond pump–probe spectroscopy at room temperature, corresponding to the distortion of the Bi–I octahedra. The coherent phonon oscillation frequency (with wavenumbers of ~97 and 130 cm⁻¹) are assigned to the symmetric stretch or bending of the BiI_6 octahedra. To the best of our knowledge, this exciton–phonon interaction of 1D chiral hybrid metal halides is reported here for the first time.

The high-quality single crystals were obtained through a cooling method by mixing stoichiometric amounts of Bi_2O_3 , Ag_2CO_3 , and an amine (*R/S/rac*-MBA) precursor in an aqueous solution of hydriodic acid at 90 °C and then slowly cooling the solution to room temperature at a cooling rate of 1 °C/h. Although a silver precursor is added to the reactant, no Ag element can be found in the crystals, which can be confirmed by single-crystal data according to single-crystal X-ray diffraction (Table 1). According to scanning electron microscope (SEM) elemental mapping (Figure S1) analysis, the Bi, I, C, and N elements are uniformly distributed, and a small amount of the Ag element is distributed on the crystal surface (Figure S1g), which originates from surface adsorption

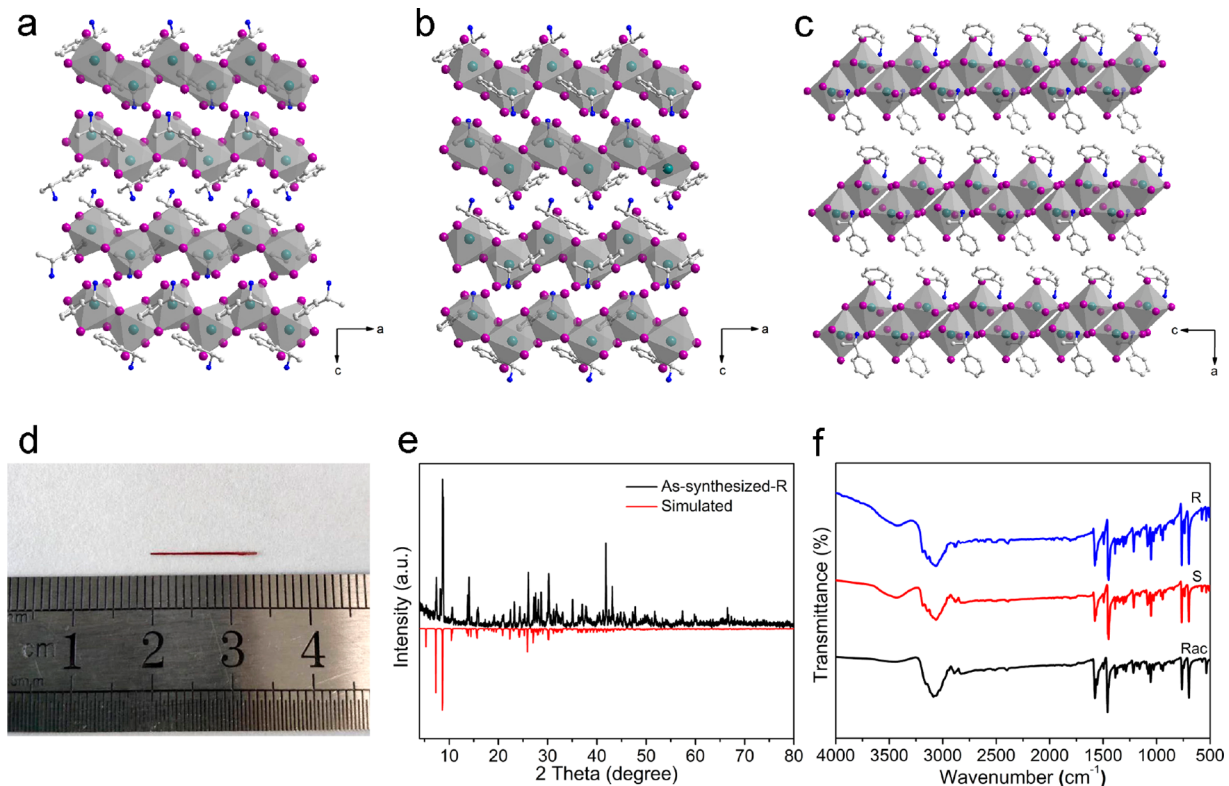


Figure 1. (a–c) Single-crystal structures of $(R\text{-MBA})_2\text{Bi}_2\text{I}_8$, $(S\text{-MBA})_2\text{Bi}_2\text{I}_8$, and $(rac\text{-MBA})_4\text{Bi}_2\text{I}_{10}$, respectively, where the green, purple, gray, and blue spheres represent Bi, I, C, and N atoms, respectively. (d) Optical images of $(R\text{-MBA})_2\text{Bi}_2\text{I}_8$. (e) PXRD patterns of $(R\text{-MBA})_2\text{Bi}_2\text{I}_8$. (f) FTIR spectra of R/S- and rac-single crystals.

of Ag atoms, consistent with X-ray photoelectron spectroscopy (XPS) characterization. The XPS survey spectra of $(R\text{-MBA})_2\text{Bi}_2\text{I}_8$ show the expected Bi, I, C, and N elements (Figure S2). The high-resolution XPS spectra show that Ag peaks cannot be observed in Figure S3a, confirming the absence of the Ag element in crystals. The doublet of 164.5 and 159.2 eV can correspond to the Bi 4f_{5/2} and 4f_{7/2} electron energy levels, respectively (Figure S3b), and the doublet of 631.3 and 619.7 eV can be attributed to the I 3d_{3/2} and 3d_{5/2} electron energy levels, respectively (Figure S3c), which confirmed the existence of the Bi–I octahedral structure. The N 1s peak also indicates the existence of chiral amine cations (Figure S3d). In addition, inductively coupled plasma (ICP) analysis (Table S1) further shows that the single-crystal structure contained only pure bismuth halide with no Ag element in it.

Crystallographic data and structural refinement information are listed in Table 1. The chiral crystal structures of $[(R\text{-MBA})_2\text{Bi}_2\text{I}_8]$ adopt the edge-sharing $[\text{BiI}_6]^{3-}$ octahedron to form a long 1D chain structure, and the chiral organic amine cations fill the void spaces (Figure 1a,b). $(rac\text{-MBA})_4\text{Bi}_2\text{I}_{10}$ was synthesized by using racemic chiral organic amine as a precursor. The difference between $(R/S\text{-MBA})_2\text{Bi}_2\text{I}_8$ and $(rac\text{-MBA})_4\text{Bi}_2\text{I}_{10}$ is that the racemic crystal is composed of two $[\text{BiI}_6]^{3-}$ octahedra by edge-sharing forming a zero-dimensional (0D) structure (Figure 1c). The incorporation of the chiral MBA cations results in a chiral space group $P2_12_12_1$ assigned to the orthorhombic crystal system for $(R/S\text{-MBA})_2\text{Bi}_2\text{I}_8$, which has only 2-fold screw symmetry, while the racemic compound phase $(rac\text{-MBA})_4\text{Bi}_2\text{I}_{10}$ crystallizes in monoclinic space group $P2_1/c$ (Table 1). The crystal of $(R\text{-MBA})_2\text{Bi}_2\text{I}_8$ is red and has a rod-like morphology, and its size

can reach $0.8 \text{ mm} \times 0.8 \text{ mm} \times 13 \text{ mm}$ (Figure 1d). The relative powder X-ray diffraction (PXRD) pattern (Figure 1e) matches well with the simulated pattern, indicating that the phases are pure. The slight difference in the intensity ratio between some PXRD peaks can be attributed to the preferred orientation of the samples during the measurement. The diffraction peak at 8.63° is assigned to the (012) crystal face, and the crystals grew with the dominant (012) plane (Figure 1e). Fourier transform infrared (FTIR) spectra of R/S- and rac-crystals are shown in Figure 1f. The peak around 3200 cm^{-1} represents the N–H bond vibration, confirming the characteristics of chiral MBA molecules in the crystal.²⁶ The thermogravimetric (TG) curve shows the crystals began to decompose at $\sim 240^\circ \text{C}$, indicating that they have a certain degree of thermal stability (Figure S4).

The crystal structures of two chiral composites are similar. The Bi atom coordinates with six adjacent I atoms, forming an octahedral structure with bond lengths ranging from 2.9060 to 3.2795 Å (Figure S5a). The I–Bi–I bond angles are in the range of $83.18\text{--}97.67^\circ$, as opposed to 90° , which confirms that the relative octahedra are distorted. However, the crystal structure of $(rac\text{-MBA})_4\text{Bi}_2\text{I}_{10}$ is similar to that of the chiral composite. The Bi–I bond lengths range from 2.9171 to 3.2524 Å, and the I–Bi–I bond angles range from 84.463° to 98.49° (Figure S5c). For the three crystals, the amines of the MBA molecule all form hydrogen bonds (N–H···I) with iodine atoms, and the hydrogen bonds significantly distort the ideal $[\text{BiI}_6]^{3-}$ octahedra. The bond length distortion index (D) is calculated to verify the degree of distortion of the Bi–I octahedron according to the following formula:³⁸

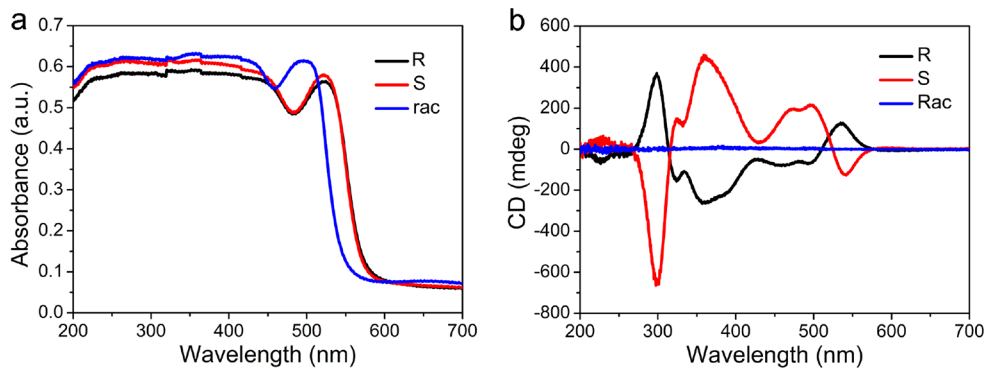


Figure 2. (a) UV–vis absorption spectrum and (b) CD spectrum of $(R/S\text{-MBA})_2\text{Bi}_2\text{I}_8$ and $(\text{rac-MBA})_4\text{Bi}_2\text{I}_{10}$ thin films.

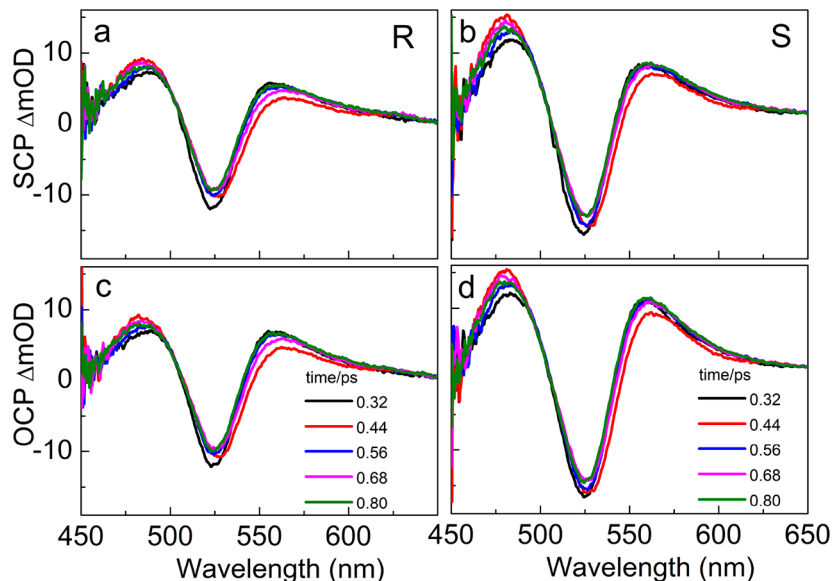


Figure 3. TA spectra of (a and b) $(R/S\text{-MBA})_2\text{Bi}_2\text{I}_8$ films and (c and d) $(R/S\text{-MBA})_2\text{Bi}_2\text{I}_8$ films with the SCP and OCP pump and probe light.

$$D = \frac{1}{6} \sum_{i=0}^6 \frac{|d_i - d_0|}{d_0}$$

where d_i represents the individual Bi–I bond lengths and d_0 is the mean Bi–I bond distance. For an ideal octahedron, D is exactly 0. The D values of R , S -, and rac -crystals are 4.2×10^{-2} , 4.2×10^{-2} , and 4.0×10^{-2} , respectively, which are significantly larger than that of the $(R\text{-MBA})_2\text{PbI}_4$ perovskite (2.1×10^{-2}).²¹ Due to the large atomic radii of Bi and I, which belong to soft acids and soft bases, they have strong covalent effects. Therefore, the polarization of the inorganic Bi–I octahedral framework is large and the 1D chiral bismuth halide has a “soft” lattice. It obviously indicates that the lattice vibrations of the “soft” crystal framework can be effectively excited by the pump light, resulting in strong exciton–phonon coupling.

As shown in Figure S6a, the solid-state ultraviolet–visible (UV–vis) diffuse reflectance spectrum shows that the absorption edge of $(R/S\text{-MBA})_2\text{Bi}_2\text{I}_8$ is \sim 665 nm and the optical bandgap (E_g) of $(R\text{-MBA})_2\text{Bi}_2\text{I}_8$ was experimentally determined to be \sim 1.86 eV (Figure S6b). To determine the band structure, we also measured the XPS valence band (VB) spectrum (Figure S7), which shows that the valence band of $(R\text{-MBA})_2\text{Bi}_2\text{I}_8$ is \sim 1.17 eV. The conduction band (CB) can be calculated as -0.69 eV in accordance with the formula CB =

$\text{VB} - E_g$. To further study the optical and chiroptical properties of the sample, we prepared the thin films of $(\text{MBA})_2\text{Bi}_2\text{I}_8$ and $(\text{MBA})_4\text{Bi}_2\text{I}_{10}$ by spin-coating of the *N,N*-dimethylformamide (DMF) and dimethyl sulfoxide (DMSO) solution of the single crystals. The UV–vis absorption spectrum of chiral films (Figure 2a) shows the 525 nm absorption peak and a broadband transition of <500 nm, which can be designated as a free exciton transition and valence band to conduction transitions, respectively.³⁹ We also noticed that there is no obvious difference in chiral films, but the absorption of the racemic samples exhibits a 25 nm blue-shift due to their different crystal structures. The CD spectrum clearly shows that the chiral thin films exhibit strong chiroptical responses and $(\text{rac-MBA})_4\text{Bi}_2\text{I}_{10}$ cannot display CD signals (Figure 2b). The characteristic mirrored CD signals indicate that they are a pair of enantiomers. In contrast to the chiral thin films, the CD spectrum of the chiral MBA molecule shows a mirrored peak at \sim 280 nm, which confirms that the CD signals below 270 nm of chiral films can be attributed to the chiroptical active transitions of the chiral MBA molecule as shown in Figure S8. The CD signals in the range of 300–600 nm can correspond to chiral structures of $(R/S\text{-MBA})_2\text{Bi}_2\text{I}_8$. The results mentioned above prove that the chirality of organic cations can be directly transferred to the inorganic Bi–I sublattice framework, endowing the corresponding hybrid $(R/S\text{-MBA})_2\text{Bi}_2\text{I}_8$ crystals

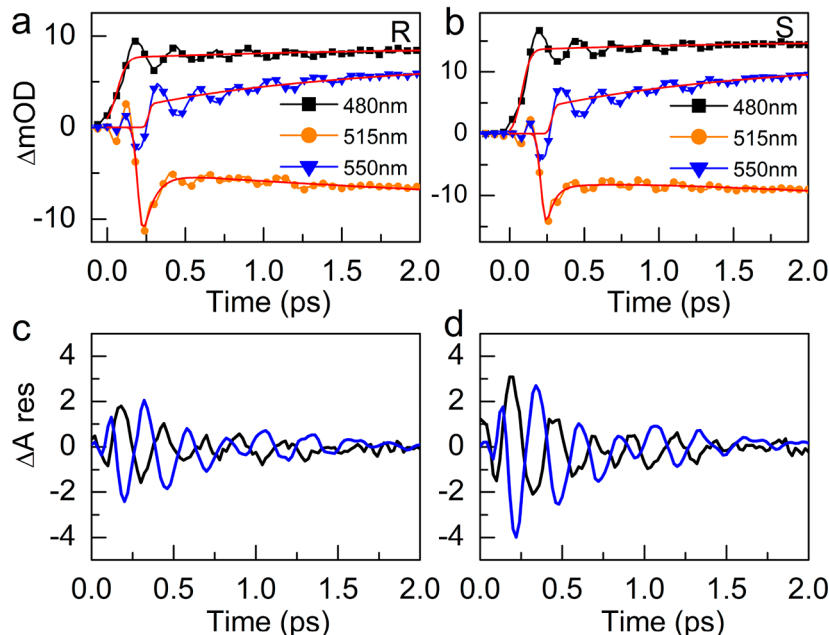


Figure 4. (a and b) TA kinetics of $(R/S\text{-MBA})_2\text{Bi}_2\text{I}_8$ films. (c and d) TA residuals of $(R/S\text{-MBA})_2\text{Bi}_2\text{I}_8$ films.

with intrinsic chirality, a case that is similar to the previously reported chiral hybrid perovskite.^{17,19,40,41}

In addition, due to the strong CD signals of more than ± 100 mdeg at 535 nm, we assume that 1D $(R/S\text{-MBA})_2\text{Bi}_2\text{I}_8$ should have a stronger chiroptical activity. However, circularly polarized photoluminescence cannot be measured in our synthesized 1D crystals due to the very low photoluminescence quantum yields at room temperature. To further investigate the physical essence of low quantum yields of 1D chiral samples, circularly polarized transient absorption (TA) spectroscopy was carried out to investigate the influential factor of low photoluminescence. We focus on the exciton–phonon coupling interactions in the following section.

In ultrafast TA measurements, a right ($\sigma+$) circularly polarized laser at 520 nm in resonance with the optical transition bands of the chiral samples was employed for the pump pulse, while a right or left ($\sigma+$ or $\sigma-$, respectively) white light continuum was used as the probe beam. The TA spectra of chiral $(R/S\text{-MBA})_2\text{Bi}_2\text{I}_8$ films with the same or opposite circular polarization (SCP or OCP, respectively) pump and probe light are displayed in Figure 3. For chiral $(R/S\text{-MBA})_2\text{Bi}_2\text{I}_8$ films, the TA spectra comprise a ground-state bleaching (GSB) signal around 525 nm and two positive photoinduced absorption (PIA) bands on both sides of the GSB band, labeled as PIA₁ (at ≈ 480 nm) and PIA₂ (at ≈ 550 nm). The origins of the GSB can be immediately assigned to the band-filling effect, while the two positive signals can be attributed to the carrier-induced broadening or bandgap renormalization.^{42,43} It is worth noting that almost identical transient features can be observed with different circularly polarized probing for both chiral films. The kinetics probed at the peaks of the GSB show similar behavior as illustrated in Figure S9. The difference between the SCP and OCP probes can be distinguished only at very early times (<300 fs). Thus, we can suggest that the spin polarization lifetime of 1D chiral $(\text{MBA})_2\text{Bi}_2\text{I}_8$ is very short. In other words, the chirality induced spin polarization does not play a major role in spin selectivity. The chiral organic spacer cannot be utilized to

enhance the spin injection and detection efficiency of 1D hybrid metal halides.⁴⁴ In fact, the fast spin relaxation can be attributed to the strong exchange Coulomb interaction, similar to what has been explored in a 2D layered perovskite ($n = 1$, where n is the average number of inorganic layers separated)^{34,45} and monolayers of semiconducting transition metal dichalcogenides.⁴⁶ In addition, the spin relaxation can also be caused by the phonon-modulated spin–orbit interaction within the Elliot–Yafet (EY) mechanism.³⁴ This result indicates that the fast spin randomization in the 1D hybrid metal halide is also induced by strong phonon scattering at room temperature.

In addition to the impact on fast exciton spin relaxation, phonons also play a crucial role in modulating the optical properties of low-dimensional metal halides. To further reveal the nature of the phonon-modulated energy states of excitons, we focus on the oscillations observed in the TA dynamics. By further analyzing the kinetics in Figure S9, we found obvious oscillations in the first picosecond, which can be commonly ascribed to the coherent interactions between the excitons and the phonons. Due to the softer nature of the hybrid metal halide, phonons in the crystal lattice can be excited by the ultrashort femtosecond pump laser, leading to a modulation of the exciton states, which can then be detected in pump–probe experiments. From a deeper analysis of the TA spectra, we found that the TA spectra show a hypochromatic shift and a bathochromic shift in the initial picoseconds. To visualize this feature, the TA residuals at 0.32, 0.44, 0.56, and 0.68 ps are shown in Figure S10. As one can see, the adjacent TA residual spectra show an antisymmetric profile, indicating that the absorption bands are modulated in energy mode rather than amplitude mode. Usually, in amplitude modulation, the absorption peak is characterized by in phase, while in energy modulation, the absorbance is characterized by an asymmetric phase centered at the transition of the exciton.³⁴ Thus, this suggests that the eigenenergies of the excitons in the 1D chiral metal halides are very easily modulated by the phonons, leading the TA spectra to shift back and forth.

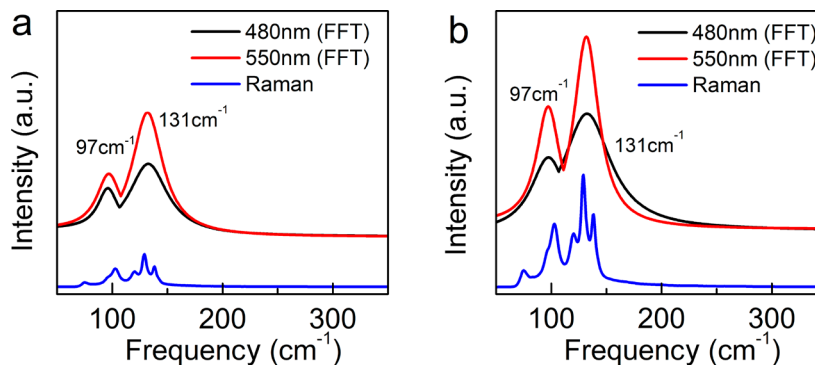


Figure 5. FFT of Δ OD residuals and Raman spectra (blue line) of (a) $(R\text{-MBA})_2\text{Bi}_2\text{I}_8$ and (b) $(S\text{-MBA})_2\text{Bi}_2\text{I}_8$.

To further explicate the phonon modulation mechanism, the dynamics probed at the peaks of the TA residuals are illustrated in panels a and b of Figure 4, in which the strongest oscillatory signals can be extracted. A periodic modulation of the TA signals can be clearly visualized by subtracting the exponentially decayed population dynamics background from the TA signals as shown in panels c and d of Figure 4. For the 1D chiral samples, the oscillation in the PIA₁ and PIA₂ region shows a nearly antisymmetric profile with a 1π phase shift. Away from the peaks of the TA residuals, the amplitude of the oscillatory signals becomes tiny (see Figure S11). It is evident that the oscillation is mainly around the exciton transition resonance.

Further insights into the strong exciton–phonon coupling for 1D chiral films were gained by fast Fourier transform (FFT). The fitted curves of FFT amplitude spectra calculated from the oscillation in panels c and d of Figure 4 are illustrated in Figure 5, in which two strong exciton–phonon modes at 97 and 131 cm⁻¹ can be identified for 1D $(R/S\text{-MBA})_2\text{Bi}_2\text{I}_8$. Until now, there had been no previous experiments or theoretical calculation on such a 1D metal halide to assign these modes, even though, referencing previous work, we can speculate that 1D, 2D, and 3D perovskites should possess similar vibrational modes because they all consist of metal halide octahedra. For example, Rao and co-workers reported exciton–phonon coupling frequencies mainly at 88 and 137 cm⁻¹ in a 2D hexylammonium lead iodide perovskite film.⁴⁷ Scopigno and co-workers also reported that, in methylammonium lead bromide perovskite, the coherent phonons modes at 98 and 137 cm⁻¹ can be assigned to the symmetric stretch of the Pb–Br octahedra, while the lower frequencies at 64 and 78 cm⁻¹ are assigned to scissoring modes.⁴⁸ Therefore, for 1D chiral $(R/S\text{-MBA})_2\text{Bi}_2\text{I}_8$, the two modes at 97 and 131 cm⁻¹ can be attributed to the symmetric stretching or bending of the BiI₆ octahedra. In contrast, the lower frequency corresponding to the bending motion of the BiI₆ octahedra cannot be observed in the FFT spectra due to a decrease in the dimension, which leads to the lack of interaction of BiI₆ octahedra along the *c*-axis.

To further address these phonon modes, we performed low-frequency Raman spectroscopy experiments on samples excited by a 633 nm laser as shown in Figure 5 (blue line). For the 1D chiral samples, an excellent match is observed at 97 cm⁻¹ between the FFT of Δ OD residuals and the Raman spectrum, while for the optical phonon modes at 131 cm⁻¹ in the FFT of TA spectra, the broad band covers three accurate vibration modes measured in the Raman spectrum. The good match between the Raman and FFT of TA spectra shows

clearly that strong exciton–phonon coupling exists in the 1D $(R/S\text{-MBA})_2\text{Bi}_2\text{I}_8$ samples. Such strong exciton–phonon interaction greatly reduces the rate of recombination of carriers at room temperature, which results in the weak photoluminescence quantum yields.

Finally, a set of parameters [Δ , S , λ] are calculated from the oscillation to quantify the phonon coupling strength. Δ , a parameter with no units, is the displacement of the normal coordinate; S is the Huang–Rhys parameter ($S = \Delta^2/2$), and λ is the reorganization energy ($\lambda = \hbar\omega_{\text{LO}}S$).^{32,33} Here, λ can be calculated from the equation $A_{\text{OSC}} = (\text{dOD}/\text{d}\omega)\Delta\omega$, where OD is the optical density of the sample and $\Delta\omega$ is the energy shift. A_{OSC} is the amplitude of the oscillations, which was obtained by fitting the Δ OD residuals to a damped sine function that was then extrapolated to time zero.³² The relevant amplitude fitting details are listed in Table S2. The calculated parameters [Δ , S , λ] for each mode of 1D $(R/S\text{-MBA})_2\text{Bi}_2\text{I}_8$ are listed in Table 2. The results show that the

Table 2. Exciton–Phonon Coupling Parameters of $(R\text{-MBA})_2\text{Bi}_2\text{I}_8$ and $(S\text{-MBA})_2\text{Bi}_2\text{I}_8$ Films

sample	ω (cm ⁻¹)	λ (meV)	S	Δ
<i>R</i>	96.8	0.44	0.04	0.28
	130.4	0.63	0.04	0.28
<i>S</i>	88.3	0.45	0.04	0.28
	131.3	0.61	0.04	0.28

Huang–Rhys factors S (~ 0.04) of 1D *R*- and *S*-(MBA)₂Bi₂I₈ are the same, which means that the connection mode of the Bi–I octahedron remains unchanged and a change in conformation will not affect the interaction between excitons and phonons. Due to the unique dielectric confinement of the 1D chiral chain structure and the large degree of Bi–I octahedral distortion, 1D chiral structures exhibit obvious exciton–phonon coupling and the coupling strength is also affected by the phonon frequency.³² Because $S < 1$ in $(R$ - and $(S\text{-MBA})_2\text{Bi}_2\text{I}_8$, large polarons may be formed.³³ Therefore, the exciton–phonon coupling in the hybrid metal halide can be achieved by adjusting the composition and structure.

Some reports have proved that the exciton–phonon coupling can be adjusted by the type of organic cation and the structure of the inorganic octahedral frame. However, the strong exciton–phonon coupling in the metal halides is a disadvantage of the light-emitting diode (LED) device, because it will result in broadening the line width and undesired asymmetric line shapes.⁴⁷ Therefore, our study of the 1D metal halide exciton–phonon interaction provides new ideas for the

design of semiconductor materials and the assembly of optoelectronic devices.

In summary, we have synthesized two lead-free chiral organic-inorganic hybrid metal halides: $(R/S\text{-MBA})_2\text{Bi}_2\text{I}_8$ and $(rac\text{-MBA})_4\text{Bi}_2\text{I}_{10}$. The Bi-I octahedral inorganic frame has a large degree of distortion and forms a 1D long chain structure via edge sharing. The ultrafast transient dynamics of chirality, spin, and exciton-phonon interaction were explicated by circularly polarized femtosecond pump-probe spectroscopy. The study found that the strong exchange Coulomb interaction and exciton-phonon coupling in 1D $(R/S\text{-MBA})_2\text{Bi}_2\text{I}_8$ led to very fast spin randomization. In particular, significant exciton-phonon coupling can be induced due to the large degree of Bi-I octahedral distortion for 1D chiral compounds at room temperature. In addition, the symmetric stretch or bending of the BiI_6 octahedra provides the dominant contribution to the coherent phonon oscillation frequency. This contribution not only explicates the obvious ultrafast coherent exciton-phonon coupling in 1D lead-free chiral hybrid metal halides but also paves a new way for phonon-based hybrid metal halide optoelectronics, such as a terahertz generator.

ASSOCIATED CONTENT

Supporting Information

The Supporting Information is available free of charge at <https://pubs.acs.org/doi/10.1021/acs.jpcllett.2c00698>.

Methods, SEM images, XPS spectra, TG curve, Bi-I octahedral structure, solid-state ultraviolet-visible diffuse reflectance spectrum, XPS valence band spectrum, CD spectrum, kinetics, TA residual spectra, ICP analysis, and oscillation amplitude fitting ([PDF](#))

Accession Codes

CCDC 2152871, 2152872, and 2152873 contain the supplementary crystallographic data for this paper. These data can be obtained free of charge via www.ccdc.cam.ac.uk/data_request/cif, or by emailing data_request@ccdc.cam.ac.uk, or by contacting The Cambridge Crystallographic Data Centre, 12 Union Road, Cambridge CB2 1EZ, UK; fax: + 44 1223 336033.

AUTHOR INFORMATION

Corresponding Authors

Hai-Yu Wang — State Key Laboratory of Integrated Optoelectronics, College of Electronic Science and Engineering, Jilin University, Changchun 130012, P. R. China;
Email: haiyu_wang@jlu.edu.cn

Hai Wang — State Key Laboratory of Integrated Optoelectronics, College of Electronic Science and Engineering, Jilin University, Changchun 130012, P. R. China;
Email: wanghai03@jlu.edu.cn

Yu Wang — State Key Laboratory of Inorganic Synthesis and Preparative Chemistry, College of Chemistry, Jilin University, Changchun 130012, P. R. China; [ORCID iD](https://orcid.org/0000-0003-3381-5006); Email: wangyu@jlu.edu.cn

Authors

Zhen Li — State Key Laboratory of Inorganic Synthesis and Preparative Chemistry, College of Chemistry, Jilin University, Changchun 130012, P. R. China

Yan Yan — State Key Laboratory of Inorganic Synthesis and Preparative Chemistry, College of Chemistry, Jilin University, Changchun 130012, P. R. China

Mu-Sen Song — State Key Laboratory of Integrated Optoelectronics, College of Electronic Science and Engineering, Jilin University, Changchun 130012, P. R. China

Jia-Yu Xin — State Key Laboratory of Inorganic Synthesis and Preparative Chemistry, College of Chemistry, Jilin University, Changchun 130012, P. R. China

Complete contact information is available at:
<https://pubs.acs.org/10.1021/acs.jpcllett.2c00698>

Notes

The authors declare no competing financial interest.

ACKNOWLEDGMENTS

This work was supported by the National Key Research and Development Program of China and the National Natural Science Foundation of China (NSFC) under Grants 21903035, 22073037, 21773087, and 21771083.

REFERENCES

- Eperon, G. E.; Leijtens, T.; Bush, K. A.; Prasanna, R.; Green, T.; Wang, J. T.; McMeekin, D. P.; Volonakis, G.; Milot, R. L.; May, R.; Palmstrom, A.; Slotcavage, D. J.; Belisle, R. A.; Patel, J. B.; Parrott, E. S.; Sutton, R. J.; Ma, W.; Moghadam, F.; Conings, B.; Babayigit, A.; Boyen, H.; Bent, S.; Giustino, F.; Herz, L. M.; Johnston, M. B.; McGehee, M. D.; Snaith, H. J. Perovskite-perovskite tandem photovoltaics with optimized band gaps. *Science* **2016**, *354*, 861–865.
- Tsai, H.; Nie, W.; Blancon, J. C.; Stoumpos, C. C.; Asadpour, R.; Harutyunyan, B.; Neukirch, A. J.; Verduzzo, R.; Crochet, J. J.; Tretiak, S.; Pedesseau, L.; Even, J.; Alam, M. A.; Gupta, G.; Lou, J.; Ajayan, P. M.; Bedzyk, M. J.; Kanatzidis, M. G.; Mohite, A. D. High-efficiency two-dimensional Ruddlesden-Popper perovskite solar cells. *Nature* **2016**, *536*, 312–316.
- Yuan, M.; Quan, L. N.; Comin, R.; Walters, G.; Sabatini, R.; Voznyy, O.; Hoogland, S.; Zhao, Y.; Beauregard, E. M.; Kanjanaboons, P.; Lu, Z.; Kim, D. H.; Sargent, E. H. Perovskite energy funnels for efficient light-emitting diodes. *Nat. Nanotechnol.* **2016**, *11*, 872–877.
- Wang, N.; Cheng, L.; Ge, R.; Zhang, S.; Miao, Y.; Zou, W.; Yi, C.; Sun, Y.; Cao, Y.; Yang, R.; Wei, Y.; Guo, Q.; Ke, Y.; Yu, M.; Jin, Y.; Liu, Y.; Ding, Q.; Di, D.; Yang, L.; Xing, G.; Tian, H.; Jin, C.; Gao, F.; Friend, R. H.; Wang, J.; Huang, W. Perovskite light-emitting diodes based on solution-processed self-organized multiple quantum wells. *Nat. Photonics* **2016**, *10*, 699–704.
- Xing, G.; Mathews, N.; Lim, S. S.; Yantara, N.; Liu, X.; Sabba, D.; Grätzel, M.; Mhaisalkar, S.; Sum, T. C. Low-temperature solution-processed wavelength-tunable perovskites for lasing. *Nat. Mater.* **2014**, *13*, 476–480.
- Zhang, Q.; Ha, S. T.; Liu, X.; Sum, T. C.; Xiong, Q. Room-Temperature Near-Infrared High-Q Perovskite Whispering-Gallery Planar Nanolasers. *Nano Lett.* **2014**, *14*, 5995–6001.
- Wei, H.; Fang, Y.; Mulligan, P.; Chuirazzi, W.; Fang, H.-H.; Wang, C.; Ecker, B. R.; Gao, Y.; Loi, M. A.; Cao, L.; Huang, J. Sensitive X-ray detectors made of methylammonium lead tribromide perovskite single crystals. *Nat. Photonics* **2016**, *10*, 333–339.
- Shi, D.; Adinolfi, V.; Comin, R.; Yuan, M.; Alarousu, E.; Buin, A.; Chen, Y.; Hoogland, S.; Rothenberger, A.; Katsiev, K.; Losovyj, Y.; Zhang, X.; Dowben, P. A.; Mohammed, O. F.; Sargent, E. H.; Bakr, O. M. Low trap-state density and long carrier diffusion in organolead trihalide perovskite single crystals. *Science* **2015**, *347*, 519–522.
- Stranks, S. D.; Eperon, G. E.; Grancini, G.; Menelaou, C.; Alcocer, M. J. P.; Leijtens, T.; Herz, L. M.; Petrozza, A.; Snaith, H. J. Electron-Hole Diffusion Lengths Exceeding 1 Micrometer in an Organometal Trihalide Perovskite Absorber. *Science* **2013**, *342*, 341–344.

- (10) Dai, S. W.; Hsu, B. W.; Chen, C. Y.; Lee, C. A.; Liu, H. Y.; Wang, H. F.; Huang, Y. C.; Wu, T. L.; Manikandan, A.; Ho, R. M.; Tsao, C. S.; Cheng, C. H.; Chueh, Y. L.; Lin, H. W. Perovskite Quantum Dots with Near Unity Solution and Neat-Film Photoluminescent Quantum Yield by Novel Spray Synthesis. *Adv. Mater.* **2018**, *30*, 1705532.
- (11) Zhu, H.; Fu, Y.; Meng, F.; Wu, X.; Gong, Z.; Ding, Q.; Gustafsson, M. V.; Trinh, M. T.; Jin, S.; Zhu, X. Y. Lead halide perovskite nanowire lasers with low lasing thresholds and high quality factors. *Nat. Mater.* **2015**, *14*, 636–642.
- (12) Zhai, Y.; Baniya, S.; Zhang, C.; Li, J.; Haney, P.; Sheng, C. X.; Ehrenfreund, E.; Vardeny, Z. V. Giant Rashba splitting in 2D organic-inorganic halide perovskites measured by transient spectroscopies. *Sci. Adv.* **2017**, *3*, e1700704.
- (13) Niesner, D.; Wilhelm, M.; Levchuk, I.; Osvet, A.; Shrestha, S.; Batentschuk, M.; Brabec, C.; Fauster, T. Giant Rashba Splitting in $\text{CH}_3\text{NH}_3\text{PbBr}_3$ Organic-Inorganic Perovskite. *Phys. Rev. Lett.* **2016**, *117*, 126401.
- (14) Mosconi, E.; Etienne, T.; De Angelis, F. Rashba Band Splitting in Organohalide Lead Perovskites: Bulk and Surface Effects. *J. Phys. Chem. Lett.* **2017**, *8*, 2247–2252.
- (15) Odenthal, P.; Talmadge, W.; Gundlach, N.; Wang, R.; Zhang, C.; Sun, D.; Yu, Z.-G.; Vary Vardeny, Z.; Li, Y. S. Spin-polarized exciton quantum beating in hybrid organic-inorganic perovskites. *Nat. Phys.* **2017**, *13*, 894–899.
- (16) Wang, J.; Zhang, C.; Liu, H.; McLaughlin, R.; Zhai, Y.; Vardeny, S. R.; Liu, X.; McGill, S.; Semenov, D.; Guo, H.; Tsuchikawa, R.; Deshpande, V. V.; Sun, D.; Vardeny, Z. V. Spin-optoelectronic devices based on hybrid organic-inorganic trihalide perovskites. *Nat. Commun.* **2019**, *10*, 129.
- (17) Ahn, J.; Lee, E.; Tan, J.; Yang, W.; Kim, B.; Moon, J. A new class of chiral semiconductors: chiral-organic-molecule-incorporating organic-inorganic hybrid perovskites. *Mater. Horiz.* **2017**, *4*, 851–856.
- (18) Huang, P. J.; Taniguchi, K.; Miyasaka, H. Bulk Photovoltaic Effect in a Pair of Chiral-Polar Layered Perovskite-Type Lead Iodides Altered by Chirality of Organic Cations. *J. Am. Chem. Soc.* **2019**, *141*, 14520–14523.
- (19) Ahn, J.; Ma, S.; Kim, J. Y.; Kyhm, J.; Yang, W.; Lim, J. A.; Kotov, N. A.; Moon, J. Chiral 2D Organic Inorganic Hybrid Perovskite with Circular Dichroism Tunable Over Wide Wavelength Range. *J. Am. Chem. Soc.* **2020**, *142*, 4206–4212.
- (20) Liu, Y.; Wang, C.; Guo, Y.; Ma, L.; Zhou, C.; Liu, Y.; Zhu, L.; Li, X.; Zhang, M.; Zhao, G. New lead bromide chiral perovskites with ultra-broadband white-light emission. *J. Mater. Chem. C* **2020**, *8*, 5673–5680.
- (21) Billing, D. G.; Lemmerer, A. Synthesis and crystal structures of inorganic–organic hybrids incorporating an aromatic amine with a chiral functional group. *CrystEngComm* **2006**, *8*, 686–695.
- (22) Long, G.; Jiang, C.; Sabatini, R.; Yang, Z.; Wei, M.; Quan, L. N.; Liang, Q.; Rasmussen, A.; Askerka, M.; Walters, G.; Gong, X.; Xing, J.; Wen, X.; Quintero-Bermudez, R.; Yuan, H.; Xing, G.; Wang, X. R.; Song, D.; Voznyy, O.; Zhang, M.; Hoogland, S.; Gao, W.; Xiong, Q.; Sargent, E. H. Spin control in reduced-dimensional chiral perovskites. *Nat. Photonics* **2018**, *12*, 528–533.
- (23) Chen, C.; Gao, L.; Gao, W.; Ge, C.; Du, X.; Li, Z.; Yang, Y.; Niu, G.; Tang, J. Circularly polarized light detection using chiral hybrid perovskite. *Nat. Commun.* **2019**, *10*, 1927.
- (24) Yuan, C.; Li, X.; Semin, S.; Feng, Y.; Rasing, T.; Xu, J. Chiral Lead Halide Perovskite Nanowires for Second-Order Nonlinear Optics. *Nano Lett.* **2018**, *18*, 5411–5417.
- (25) Yang, C. K.; Chen, W. N.; Ding, Y. T.; Wang, J.; Rao, Y.; Liao, W. Q.; Tang, Y. Y.; Li, P. F.; Wang, Z. X.; Xiong, R. G. The First 2D Homochiral Lead Iodide Perovskite Ferroelectrics: [R- and S-1-(4-Chlorophenyl)ethylammonium]₂PbI₄. *Adv. Mater.* **2019**, *31*, 1808088.
- (26) Hu, Y.; Florio, F.; Chen, Z.; Phelan, W. A.; Siegler, M. A.; Zhou, Z.; Guo, Y.; Hawks, R.; Jiang, J.; Feng, J.; Zhang, L.; Wang, B.; Wang, Y.; Gall, D.; Palermo, E. F.; Lu, Z.; Sun, X.; Lu, T.-M.; Zhou, H.; Ren, Y.; Wertz, E.; Sundararaman, R.; Shi, J. A chiral switchable photovoltaic ferroelectric 1D perovskite. *Sci. Adv.* **2020**, *6*, eaay4213.
- (27) Di Nuzzo, D.; Cui, L.; Greenfield, J. L.; Zhao, B.; Friend, R. H.; Meskers, S. C. J. Circularly Polarized Photoluminescence from Chiral Perovskite Thin Films at Room Temperature. *ACS Nano* **2020**, *14*, 7610–7616.
- (28) Dang, Y.; Liu, X.; Sun, Y.; Song, J.; Hu, W.; Tao, X. Bulk Chiral Halide Perovskite Single Crystals for Active Circular Dichroism and Circularly Polarized Luminescence. *J. Phys. Chem. Lett.* **2020**, *11*, 1689–1696.
- (29) Gao, J.-X.; Zhang, W.-Y.; Wu, Z.-G.; Zheng, Y.-X.; Fu, D.-W. Enantiomeric Perovskite Ferroelectrics with Circularly Polarized Luminescence. *J. Am. Chem. Soc.* **2020**, *142*, 4756–4761.
- (30) Wright, A. D.; Verdi, C.; Milot, R. L.; Eperon, G. E.; Pérez-Osorio, M. A.; Snaith, H. J.; Giustino, F.; Johnston, M. B.; Herz, L. M. Electron–Phonon Coupling in Hybrid Lead Halide Perovskites. *Nat. Commun.* **2016**, *7*, 11755.
- (31) Debnath, T.; Sarker, D.; Huang, H.; Han, Z. K.; Dey, A.; Polavarapu, L.; Levchenko, S. V.; Feldmann, J. Coherent vibrational dynamics reveals lattice anharmonicity in organic-inorganic halide perovskite nanocrystals. *Nat. Commun.* **2021**, *12*, 2629.
- (32) Fu, J.; Li, M.; Solanki, A.; Xu, Q.; Lekina, Y.; Ramesh, S.; Shen, Z. X.; Sum, T. C. Electronic States Modulation by Coherent Optical Phonons in 2D Halide Perovskites. *Adv. Mater.* **2021**, *33*, 2006233.
- (33) Ghosh, T.; Aharon, S.; Etgar, L.; Ruhman, S. Free Carrier Emergence and Onset of Electron–Phonon Coupling in Methylammonium Lead Halide Perovskite Films. *J. Am. Chem. Soc.* **2017**, *139*, 18262–18270.
- (34) Giovanni, D.; Chong, W. K.; Liu, Y. Y. F.; Dewi, H. A.; Yin, T.; Lekina, Y.; Shen, Z. X.; Mathews, N.; Gan, C. K.; Sum, T. C. Coherent Spin and Quasiparticle Dynamics in Solution-Processed Layered 2D Lead Halide Perovskites. *Adv. Sci.* **2018**, *5*, 1800664.
- (35) Xu, X.; Zhang, X.; Deng, W.; Jie, J.; Zhang, X. 1D Organic–Inorganic Hybrid Perovskite Micro/Nanocrystals: Fabrication, Assembly, and Optoelectronic Applications. *Small Methods* **2018**, *2*, 1700340.
- (36) Rahaman, Md. Z.; Ge, S.; Lin, C. H.; Cui, Y.; Wu, T. One-Dimensional Molecular Metal Halide Materials: Structures, Properties, and Applications. *Small Struct.* **2021**, *2*, 2000062.
- (37) Thouin, F.; Valverde-Chavez, D. A.; Quart, C.; Cortecchia, D.; Bargigia, I.; Beljonne, D.; Petrozza, A.; Silva, C.; Srimath Kandala, A. R. Phonon coherences reveal the polaronic character of excitons in two-dimensional lead halide perovskites. *Nat. Mater.* **2019**, *18*, 349–356.
- (38) Lu, H.; Xiao, C.; Song, R.; Li, T.; Maughan, A. E.; Levin, A.; Brunecky, R.; Berry, J. J.; Mitzi, D. B.; Blum, V.; Beard, M. C. Highly Distorted Chiral Two-Dimensional Tin Iodide Perovskites for Spin Polarized Charge Transport. *J. Am. Chem. Soc.* **2020**, *142*, 13030–13040.
- (39) Yao, L.; Zeng, Z.; Cai, C.; Xu, P.; Gu, H.; Gao, L.; Han, J.; Zhang, X.; Wang, X.; Wang, X.; Pan, A.; Wang, J.; Liang, W.; Liu, S.; Chen, C.; Tang, J. Strong Second- and Third-Harmonic Generation in 1D Chiral Hybrid Bismuth Halides. *J. Am. Chem. Soc.* **2021**, *143*, 16095–16104.
- (40) Ma, J.; Fang, C.; Chen, C.; Jin, L.; Wang, J.; Wang, S.; Tang, J.; Li, D. Chiral 2D Perovskites with a High Degree of Circularly Polarized Photoluminescence. *ACS Nano* **2019**, *13*, 3659–3665.
- (41) Li, D.; Liu, X.; Wu, W.; Peng, Y.; Zhao, S.; Li, L.; Hong, M.; Luo, J. Chiral Lead-Free Hybrid Perovskites for Self-Powered Circularly Polarized Light Detection. *Angew. Chem., Int. Ed.* **2021**, *60*, 8415–8418.
- (42) Tao, W.; Zhou, Q.; Zhu, H. Dynamic Polaronic Screening for Anomalous Exciton Spin Relaxation in Two-Dimensional Lead Halide Perovskites. *Sci. Adv.* **2020**, *6*, eabb7132.
- (43) Zhao, W.; Su, R.; Huang, Y.; Wu, J.; Fong, C. F.; Feng, J.; Xiong, Q. Transient circular dichroism and exciton spin dynamics in all-inorganic halide perovskites. *Nat. Commun.* **2020**, *11*, 5665.

- (44) Ma, S.; Ahn, J.; Moon, J. Chiral Perovskites for Next-Generation Photonics: From Chirality Transfer to Chiroptical Activity. *Adv. Mater.* **2021**, *33*, 2005760.
- (45) Chen, X.; Lu, H.; Li, Z.; Zhai, Y.; Ndione, P. F.; Berry, J. J.; Zhu, K.; Yang, Y.; Beard, M. C. Impact of Layer Thickness on the Charge Carrier and Spin Coherence Lifetime in Two-Dimensional Layered Perovskite Single Crystals. *ACS Energy Lett.* **2018**, *3*, 2273–2279.
- (46) Schmidt, R.; Berghäuser, G.; Schneider, R.; Selig, M.; Tonndorf, P.; Malić, E.; Knorr, A.; Michaelis de Vasconcellos, S.; Bratschitsch, R. Ultrafast coulomb-induced intervalley coupling in atomically thin WS₂. *Nano Lett.* **2016**, *16*, 2945–2950.
- (47) Ni, L.; Huynh, U.; Cheminal, A.; Thomas, T. H.; Shivanna, R.; Hinrichsen, T. F.; Ahmad, S.; Sadhanala, A.; Rao, A. Real-Time Observation of Exciton–Phonon Coupling Dynamics in Self-Assembled Hybrid Perovskite Quantum Wells. *ACS Nano* **2017**, *11*, 10834–10843.
- (48) Batignani, G.; Fumero, G.; Srimath Kandada, A. R.; Cerullo, G.; Gandini, M.; Ferrante, C.; Petrozza, A.; Scopigno, T. Probing femtosecond lattice displacement upon photo-carrier generation in lead halide perovskite. *Nat. Commun.* **2018**, *9*, 1971.

□ Recommended by ACS

Temperature-Dependent Optical and Structural Properties of Chiral Two-Dimensional Hybrid Lead-Iodide Perovskites

Ibrahim Dursun, Qiuming Yu, *et al.*

AUGUST 02, 2023

THE JOURNAL OF PHYSICAL CHEMISTRY C

READ

Origin of Broad Emission Induced by Rigid Aromatic Ditopic Cations in Low-Dimensional Metal Halide Perovskites

Marta Morana, Lorenzo Malavasi, *et al.*

AUGUST 28, 2023

THE JOURNAL OF PHYSICAL CHEMISTRY LETTERS

READ

Uncovering Multiple Intrinsic Chiral Phases in (PEA)₂PbI₄ Halide Perovskites

Shahar Zuri, Efrat Lifshitz, *et al.*

MAY 18, 2023

THE JOURNAL OF PHYSICAL CHEMISTRY LETTERS

READ

Ultraviolet–Visible–Near-Infrared Photoresponses Realized in a Polar Dion–Jacobson Hybrid Perovskite through Light-Induced Pyroelectric Effects

Zhuo Chen, Dongying Fu, *et al.*

SEPTEMBER 29, 2023

CHEMISTRY OF MATERIALS

READ

Get More Suggestions >